frontiers in Earth Science

ORIGINAL RESEARCH
published: 03 September 2021
doi: 10.3389/feart.2021.711706

Rockburst Prediction From the Perspective of Energy Release: A Case Study of a Diversion Tunnel at Jinping II Hydropower Station

Yong Fan[1,2,3], *Xianze Cui*[1], *Zhendong Leng*[1,4], *Junwei Zheng*[1]*, *Feng Wang*[1] *and Xiaole Xu*[1]

[1]Hubei Key Laboratory of Construction and Management in Hydropower Engineering, China Three Gorges University, Yichang, China, [2]Key Laboratory of Rock Mechanics in Hydraulic Structural Engineering, Ministry of Education, Wuhan University, Wuhan, China, [3]Key Laboratory of Geological Hazards on Three Gorges Reservoir Area of Ministry of Education, China Three Gorges University, Yichang, China, [4]China Gezhouba Group Explosive Co.Ltd, Chongqing, China

As a man-made engineering hazard, it is widely accepted that the rockbursts are the result of energy release. Previous studies have examined the unloading of *in-situ* stress resulting from deep tunnel excavation as a quasi-static process but the transient stress variation during excavation has received less attention. This research discusses rockbursts that happened during the construction of a diversion tunnel at Jinping II hydropower station. The brittle-ductile-plastic (BDP) transition property of Jinping marble was numerically described by the Hoek-Brown strength criterion, and the dynamic energy release process derived from the transient unloading of *in-situ* stress was studied using an index, local energy release rate. Studies have shown that, due to transient unloading, the strain energy of the surrounding rock mass goes through a dynamic process of decreasing at first, increasing second, then reducing before finally stabilizing. The first decrease of strain energy results from elastic unloading waves and does not cause brittle failure in rock masses, which is consistent with the elastic condition but the secondary reduction of strain energy is because the accumulated strain energy in rock masses exceeds the storage limit, which will inevitably trigger the brittle failure in the rock mass. Thus, the shorter the distance to the tunnel wall the bigger and more intense the energy release. Finally, a relationship between the average value of the local energy release rate and the rockburst intensity was established to assess the risk of rockburst induced by the blasting excavation of a deep tunnel.

Keywords: high *in-situ* stress, energy release, rockburst, transient unloading, deep tunnel

OPEN ACCESS

Edited by:
Faming Huang,
Nanchang University, China

Reviewed by:
Jianhua Yang,
Nanchang University, China
Meysam Imani,
Amirkabir University of Technology, Iran

***Correspondence:**
Junwei Zheng
jjunweizheng@163.com

Specialty section:
This article was submitted to Environmental Informatics and Remote Sensing, a section of the journal Frontiers in Earth Science

Received: *19 May 2021*
Accepted: *08 July 2021*
Published: *03 September 2021*

Citation:
Fan Y, Cui X, Leng Z, Zheng J, Wang F and Xu X (2021) Rockburst Prediction From the Perspective of Energy Release: A Case Study of a Diversion Tunnel at Jinping II Hydropower Station. Front. Earth Sci. 9:711706. doi: 10.3389/feart.2021.711706

1 INTRODUCTION

To take full advantage of hydropower in Southwest China, a large number of hydropower stations have been constructed. However, restricted by the narrow terrain conditions in western China, most of these projects need a large-scale excavation of underground caverns to create space for the arrangement of hydraulic structures. Because of the large burial depth, the rock mass of the excavation area is characterized by high *in-situ* stress, after excavation, it may induce the damage and failure of the surrounding rock mass or even cause man-made engineering disasters, rockbursts (Cook, 1976; Kisslinger, 1976; Martino and Chandler, 2004; Read, 2004; Alija et al., 2013; Alija et al., 2014; Feng et al.,

2018a; Feng et al., 2018b). A good deal of numerical studies, laboratory tests, and theoretical analyses have claimed that the damage or failure of rock masses after excavation is a comprehensive behaviour of energy dissipation and energy release. Among them, the damage of rock masses mainly results from energy dissipation, and the dynamic failure of rock masses and the rockburst are mainly induced by the energy release (Hodgson and Joughin, 1966; Toksöz and Kehrer, 1972; Singh, 1988; Mikhalyuk and Zakharov, 1997; Wang and Park, 2001; He et al., 2010; Su et al., 2017; Su et al., 2018; Chen et al., 2019). Thus, exploring the energy release regularities of the rock mass around the excavation boundary derived from the tunnel excavation is crucial for revealing the evolution mechanism of underground engineering hazards such as rockbursts.

As early as 1966, a new index, energy release rate, was proposed to solve rockburst problems in a South African gold mine (Cook et al., 1966). It was not until 1977 that Walsh systematically completed the description of variation regularities of the surrounding rock mass energy under the action of excavation (Walsh, 1977). Afterwards, Brady and Brown studied the internal connection of the energy variation and the stability of the surrounding rock mass after excavation by using the boundary element method (Brady and Brown, 1981). During the tunnel excavation, the energy system is composed of five parts under elastic and continuous conditions. The energy consumed by external and body forces, the energy consumed by support or backfill, the energy released during excavation, the energy of the excavated rock mass, the increased energy of the surrounding rock mass (Salamon, 1983). Moreover, these five parts in the above energy system can be transformed into each other under the influence of excavation disturbance (Salamon, 1984). On this basis, the energy change regularity during the expansion of the explosion gas in the complex structural surface and the energy release regularity due to mining under different excavation footage were studied (Napier, 1991; Mitri et al., 1999). To better explain the energy change behaviour of rock masses during tunnel excavation, the concepts of energy flow line and energy flow vector were proposed by Kramarenko and Revuzhenko to analyze the energy change regularity induced by tunnel excavation (Kramarenko and Revuzhenko, 1998). After that, Revuzhenko and Klishin found that the characteristic of the energy flow line is mainly affected by the excavation boundary (Revuzhenkor and Klishin, 2009). Due to the tunnel excavation, the energy transmits with the energy flow line from the external boundary to the excavation boundary, which will cause the energy accumulation near the excavation boundary (Lindin and Lobanova, 2013).

The above studies revealed the variation regularity of the rock mass energy resulted from tunnel excavation. However, most of these studies posited that the tunnel excavation induced *in-situ* stress unloading under the deeply buried depth as a process of final quasi-static stress distribution. Recent studies have shown that the duration of the stress unloading process on the excavation boundary is within only a few milliseconds by analyzing the broken process of the rock mass in the excavation area and monitoring the stress change path of the rock mass around the excavation surface. During this short and rapid process, the tunnel excavation induced *in-situ* stress unloading and cannot be regarded as a process of final quasi-static stress distribution but a transient and dynamic process, and the dynamic effect induced by the transient stress unloading will cause different stress and energy variation behaviours in the surrounding rock mass, which should not be ignored in the analysis (Lu et al., 2012; Li et al., 2014; Zhu et al., 2014; Fan et al., 2015; Yang et al., 2016; Yang et al., 2018; Fan et al., 2021). This research aims to reveal the regularity of energy release derived from the transient stress unloading and set up an association of the energy release and the rockburst intensity for deep tunnels during blasting excavation. To accomplish this goal, the rockbursts that took place in the No.2 diversion tunnel of Jinping II hydropower station during blasting excavation are first introduced. The special mechanical properties of Jinping marble were simulated by employing Hoek-Brown strength criterion in Fast Lagrangian Analysis of Continua 3D (FLAC 3D), and a BDP model of Jinping marble was established. Using the BDP model. We then studied the dynamic process of the energy release caused by the blasting excavation induced transient unloading of a deep-buried tunnel. Finally, a relationship between the average value of the local energy release rate and the rockburst intensity was established to predict the rockburst risk.

2 ROCKBURSTS IN THE DIVERSION TUNNEL OF JINPING II HYDROPOWER STATION DURING BLASTING EXCAVATION

2.1 Geological Conditions

Jinping II hydropower station was constructed on the lower half of the Yalong River bend in Sichuan Province, China. It is one of the most important cascade hydropower stations on the mainstream of Yalong River (**Figure 1A**). To utilize the highly natural drop for power generation, the river bend with a length of 150 km is cut by several underground tunnels. Among them, the length of the diversion tunnel is about 17 km, and the buried depth of the overlying rock mass reaches 1,500–2000 m. The circular section designed with a diameter of 12.4 m was adopted for the construction of No. 1 and No. 3 diversion tunnels using a tunnel boring machine (TBM), and a horseshoe section designed with a diameter of 13.0 m was used for the construction of No. 2 and No. 4 diversion tunnels by employing blasting. To avoid construction interference, a 60 m parallel interval between each diversion tunnel was designed as shown in **Figure 1A**.

1) Stratigraphic Lithology

Along the diversion tunnels, the main lithology of the strata is marble, slate, sandstone, and limestone. Along the reverse water flow direction of the diversion tunnels, they are Yantang Formation (T_{2y}), Baishan Formation (T_{2b}), Triassic Upper Series (T_3), Zagunao Formation (T_{2z}), and Triassic Lower Series (T_1), respectively (**Figure 1B**). Among them, the Yantang Formation (T_{2y}) mainly distributes in the Dashuigou area, and the core of the Laozhuangzi anticline is composed of marble and argillaceous limestone. The marble of the Baishan

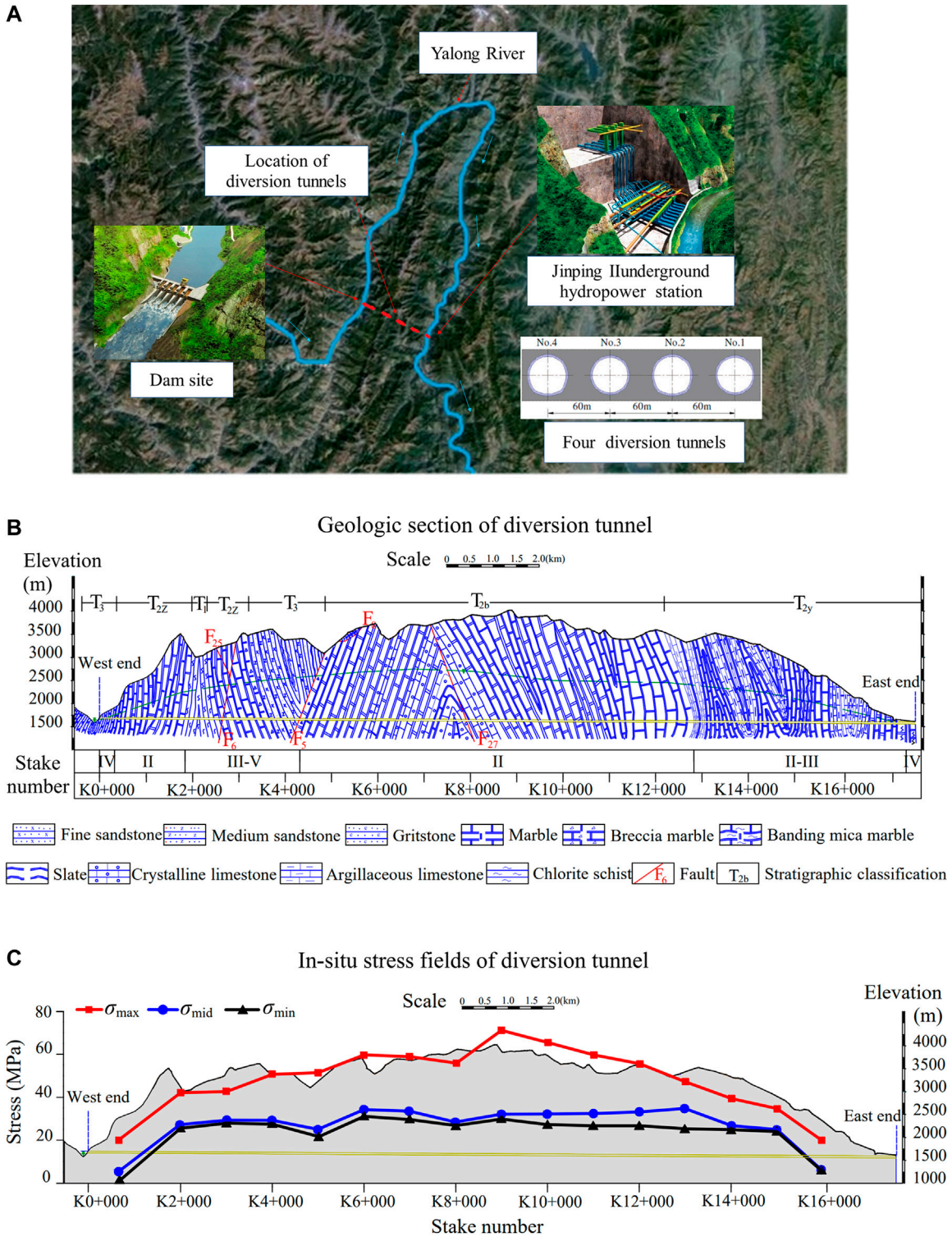

FIGURE 1 | Geological Conditions. **(A)** Location of the diversion tunnels at Jinping II hydropower, **(B)** Geologic section of the diversion tunnels at Jinping II hydropower project, **(C)** *In-situ* stress fields of the diversion tunnels at Jinping II hydropower project.

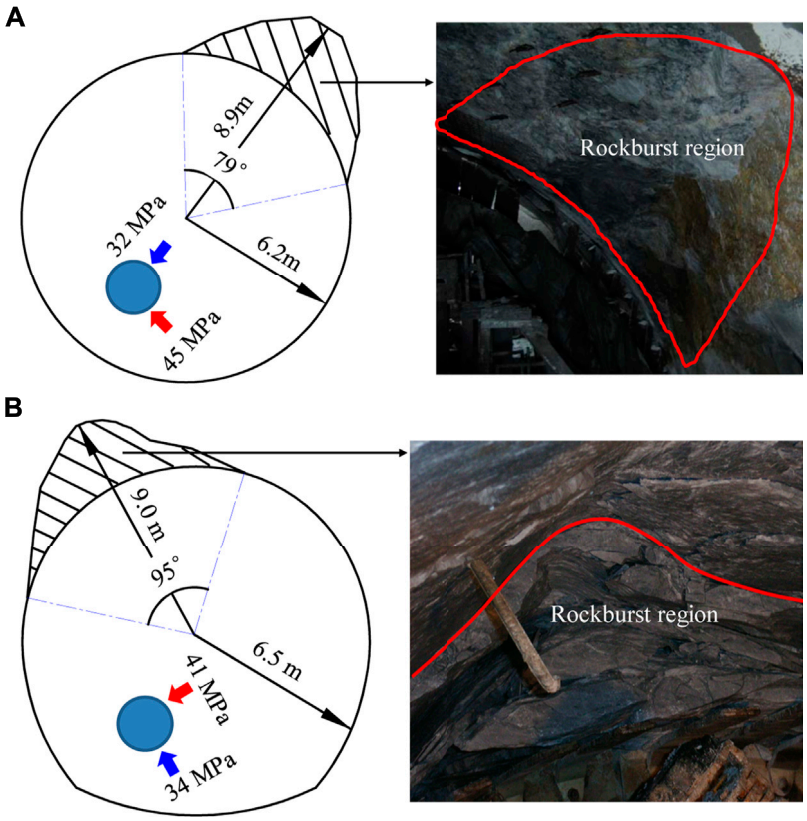

FIGURE 2 | Rockburst occurred during excavation of diversion tunnels at Jinping II hydropower project. **(A)** At No. 1 diversion tunnel, **(B)** At No. 2 diversion tunnel.

Formation (T_{2b}) mainly distributes in the middle of the project area, which forms the main part of the Jinping Mountains. The Baishan marble (T_{2b}) is stable and compact, and the thickness of the whole layer is 750–2,270 m. The Upper Triassic (T_3) mainly distributes in the main watershed, and its lithology is sandstone and slate. The Lower Triassic (T_1) stratum mainly distributes in the western part of the tunnel area, and its lithology is complex, which is composed of biotite chlorite schist, metamorphic medium-fine sandstone with thin-bedded marble, gravel or banded marble, etc.

2) Geological structure

In the project area, the folds are extremely developed and complicated, and most of them are dense folds extending near the SN direction (NNE). Generally, these folds are composed of three belts: east, middle, and west. Through the geological survey, it is revealed that compression bedding and NE-trending thrust faults are the main structural planes in the project area. Based on different structural features and distribution orientations, these planes are classified into four tectonic groups: NNW, NNE, NW~NWW, and NE~NEE. The main faults that the diversion tunnel passed through are F_5, F_6, F_{25}, and F_{27}, which are shown in **Figure 1B**. The attitude of F_5 fault is N10°~30°E, NW∠70°, with an affecting width of 5–10 m. The occurrence of the fault F_6 is N20°~50°E, NW or SE∠60°~87°with the bandwidth of 1–4.2 m. The attitude of the F_{27} fault tends to the N30~40°W direction, which is located in the middle of the Ganhaizi Formation and distributes in the Baishan Formation (T_{2b}). The attitude of the fault F_{25} is N20°E, SE∠70°with a crushing bandwidth of 1–2 m.

3) *In-situ* stress fields

Because of the complex geological conditions and large burial depth, the *in-situ* stress at the construction area of four diversion tunnels is relatively high. Using the hydraulic fracturing method, the *in-situ* stress field at the construction area was measured (see **Figure 1C**). From **Figure 1C**, the maximum principal stress (σ_{max}) reaches 72 MPa with a dip angle of 6.45–75.4°. The middle principal stress (σ_{mid}) reaches 34 MPa with a dip angle of 25°and is approximately perpendicular to the tunnel axis. For the minimum principal stress (σ_{min}), it reaches about 29 MPa in the vertical direction with a dip angle of 65°.

2.2 Rockburst Characteristics Occurred at No. 2 Diversion Tunnel

In the tunnel area, the lithology of the rock mass is mostly pure and brittle marble with high strength. Due to the large burial depth, the rock mass is endowed with high *in-situ* stress. These

TABLE 1 | Rockbursts occurred at No. 2 diversion tunnel from stake number K10+600 to K17+000.

Tunnel stake number (K)		Length in axis (m)	Location at cross-section	Form	type	Crater depth (cm)	Grade
10+600	10+626	26	Right side	Exfoliation	Slight	10~50	I
10+644	10+658	14	Right side	Exfoliation	Slight	10~30	I
10+658	10+664	6	Right side	Exfoliation	Slight	50	I
10+664	10+688	24	Right side	Plate peeling	Slight	30~50	I
10+688	10+712	24	Right side	Plate peeling	Medium	50~80	II
10+712	10+744	32	Right side	Plate peeling	Medium	60~100	II
10+747	10+780	33	Right side to spandrel	Lump flick	Slight	30~50	I
10+780	10+852	72	Right side to spandrel	Lump flick	Medium	30~80	II
10+871	10+880	9	Left side to spandrel	Lump flick	Medium	80	II
10+880	10+893	13	Right side to spandrel	Lump flick	Intense	150~280	III
10+900	10+948	48	Left spandrel	Lump peeling	Slight	30~70	II
10+948	10+978	30	Right side to spandrel	Lump flick	Medium	30~100	II
10+978	11+006	28	Right side to spandrel	Lump flick	Intense	150~220	III
11+006	11+017	11	Right side to spandrel	Lump flick	Drastic	150~300	IV
11+017	11+046	29	Right side to spandrel	Lump flick	Intense	150~250	III
11+046	11+076	30	Right side to spandrel	Lump spalling	Medium	50~100	II
11+076	11+112	36	Right side to spandrel	Plate peeling	Slight	10~30	I
11+116	11+126	10	Right side to spandrel	Plate peeling	Slight	20~30	I
11+236	11+262	26	Right side to spandrel	Plate peeling	Slight	10~30	I
11+269	11+282	13	Right side to spandrel	Plate peeling	Slight	10~40	I
11+284	11+294	10	Right side to spandrel	Lump spalling	Medium	30~100	II
11+302	11+349	47	Right side to spandrel	Lump spalling	Medium	50~100	II
11+352	11+377	25	Right side to spandrel	Lump spalling	Medium	50~120	II
11+380	11+412	32	Right side to spandrel	Lump spalling	Medium	50~100	II
11+447	11+466	19	Right side to spandrel	Stratiform peeling	Slight	10~50	I
11+498	11+503	5	Left side to spandrel	Stratiform peeling	Slight	50	I
11+580	11+585	5	Left side to spandrel	Stratiform peeling	Slight	30	I
11+659	11+677	18	Right side to spandrel	Stratiform peeling	Slight	10~40	I
11+890	11+897	7	Right side to spandrel	Stratiform peeling	Slight	5	I
11+900	11+915	15	Right side to spandrel	Stratiform peeling	Slight	10~50	I
11+916	11+919	3	Left spandrel	Lump peeling	Slight	10~20	I
11+919	11+932	13	Right side to spandrel	Stratiform peeling	Slight	10~50	I
11+935	11+947	12	Right side to spandrel	Stratiform peeling	Slight	10~50	I
11+947	11+957	10	Right side to spandrel	Stratiform peeling	Slight	10	I
12+617	12+624	7	Left spandrel	Lump collapse	Medium	20~100	II
12+644	12+690	46	Left spandrel to top	Lump collapse	Medium	10~150	II
12+732	12+736.5	4.5	top	Rib spalling	Slight	10~30	I
12+740	12+751	11	Left spandrel	Rib spalling	Slight	10~40	I
12+800	12+817	17	Right spandrel	Rib spalling	Slight	10~50	I
12+849	12+867	18	Spandrel and Right side	Peeling	Medium	10~240	II
12+867	12+871	4	Right spandrel	Rib spalling	Slight	10~20	I
13+034	13+056	22	Left side to spandrel	Peeling	Medium	20~100	II
13+056	13+064.5	8.5	Right side	Rib spalling	Slight	10~50	I
13+065	13+070.5	5.5	Right spandrel	Rib spalling	Slight	10	I
13+146	13+150	4	Right spandrel	Rib spalling	Slight	10~30	I
13+161	13+168.5	7.5	Top	Rib spalling	Slight	10~28	I
13+211	13+226	15	Top and right spandrel	Rib spalling	Slight	10~43	I
13+360	13+367	7	Right side and spandrel	Rib spalling	Medium	20~80	II
14+156	14+172	16	Top	Peeling	Slight	30	I
14+189	14+216	27	Right spandrel	Peeling	Slight	10~32	I
14+218	14+227	9	Left side	Peeling	Slight	10~15	I
14+234	14+240	6	Left side	Peeling	Slight	10~20	I
14+580	14+587	7	Left spandrel	Falling	Medium	80	II
14+644	14+646	2	Left spandrel	Peeling	Slight	40	I
14+708	14+714	6	Right side	Peeling	Slight	50	I
14+832	14+842	10	Right side	Peeling	Slight	50	I
15+053	15+055	2	Right side	Peeling	Slight	15	I
15+055	15+058	3	Right side	Peeling	Slight	15	I
15+068	15+079	11	Right side	Falling	Slight	40	I
15+093	15+099	6	Left spandrel	Falling	Slight	10~25	I
15+121	15+122	1	Left spandrel	Peeling	Slight	5	I
15+288	15+295	7	Right spandrel	Falling	Medium	100	I
15+323	15+338	15	Right spandrel	Peeling	Slight	10	I

(Continued on following page)

TABLE 1 | (*Continued*) Rockbursts occurred at No. 2 diversion tunnel from stake number K10+600 to K17+000.

Tunnel stake number (K)		Length in axis (m)	Location at cross-section	Form	type	Crater depth (cm)	Grade
15+353	15+355	2	Top	Peeling	Slight	10	I
15+374	15+376	2	Right spandrel	Peeling	Slight	10	I
15+420	15+426	6	Left spandrel	Peeling	Slight	10	I
15+426	15+432	6	Right spandrel	Peeling	Slight	10	I
15+458	15+463	5	Top	Peeling	Slight	10	I
15+480	15+484	4	Left side	Falling	Slight	10	I
16+066	16+070	4	Right spandrel	Peeling	Slight	20	I
16+071	16+076	5	Left spandrel	Peeling	Slight	30	I
16+081	16+086	5	Left spandrel	Peeling	Slight	30	I
16+091	16+095	4	Left spandrel	Exfoliation	Slight	30	I
16+095	16+097	2	Left spandrel	Exfoliation	Slight	30	I
16+411	16+413	2	Top	Exfoliation	Slight	30	I

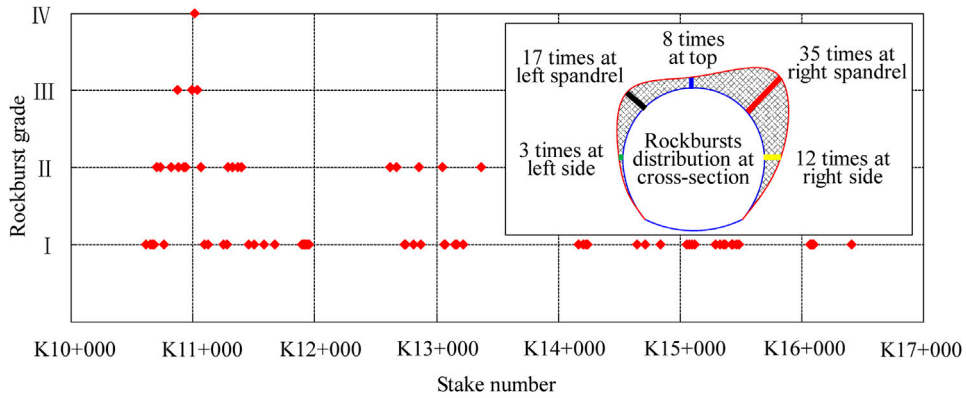

FIGURE 3 | Rockburst grade along the tunnel axis and rockburst frequency at the tunnel cross-section.

two factors constitute the basic conditions for the occurrence of rockbursts. Subsequently, influenced by the blasting excavation induced disturbance, the rockburst occurred frequently (**Figure 2**).

To analyze the evolution mechanism of rockbursts induced by blasting excavation, the rockbursts that occurred at No. 2 diversion tunnel from stake number K10+600 to K17+000 were observed and recorded, as shown in **Table 1**. Otherwise, the rockburst intensity at the No.2 diversion tunnel and the rockburst frequency around the tunnel cross-section is given in **Figure 3**. According to **Figure 3**, there were 75 rockbursts during the blasting excavation of No. 2 diversion tunnel from stake number K10+600 to K17+000, and the majority of the rockbursts forms were exfoliation, lump flick, and peeling. From the field observation, the surface of the rockburst crater is fresh, showing the characteristics of "shallow pit", "deep pit" and "V-shape". The crater length of the rockburst at the No.2 diversion tunnel ranges from 1 m to 72 m, and the crater depth of the strongest rockburst reached 1.5~3.0 m. According to the length and depth of the rockburst crater, the rockburst intensity is mainly divided into four grades: slight rockburst (I), medium rockburst (II), intense rockburst (III), and drastic rockburst (IV). Among these four grades, the different rockburst grades correspond to the different sizes of rock fragments. In general, the higher the rockburst grade means the deeper crater, the larger size of rock fragments, the farther the ejection distance of rock fragments caused by rockbursts, and the louder the sound produced by rockbursts.

Combined with **Table 1**, **Figures 1B,C** and **Figure 3**, the frequency and intensity of the rockbursts that took place near the stake number K11+000 were more drastic than those that took place near stake number K16+000, which indicates that rockbursts tend to occur around the tunnel cross-section with high *in-situ* stress and buried depth. Since No. 2 diversion tunnel was excavated by the upper and lower step method, almost all of the rockbursts happened at the upper section of the tunnel. Among the total frequency of the rockbursts that happened at the No.2 diversion tunnel, 35 rockbursts took place at the right spandrel, and 17 rockbursts occurred at the left spandrel. In addition, 12, 8, and 3 rockbursts happened at the right side, top and left side of the tunnel cross-sections, respectively.

From **Figures 1B,C** and **Figure 3**, we can also find that from stake number K16+000 to K11+000, the intensity, frequency, and rockburst grade enlarge with the increase of burial depth. Furthermore, it can also be seen from the figures that the burial depth is not the only influencing factor. There is a close

correspondence between the rockburst frequency and the geological structure (syncline, anticline) along the tunnel axis, which indicates that the impact of geological structures on the *in-situ* stress field is another important factor that induces rockbursts. To facilitate the classification of rockbursts, we regarded the sporadic rockburst and continuous rockburst as the low-grade rockburst and high-grade rockburst, respectively. Generally, the intensity and grade of rockbursts are closely related to the level of *in-situ* stress.

When excavating No. 2 diversion tunnel by blasting, rockbursts happened frequently, which caused work stoppage more than once and increased the lining and support costs. As a man-made engineering disaster, rockbursts are not only harmful to the stability of the rock mass near the excavation area, they also threaten the security of workers and mechanical equipment near the occurrence area. Thus, it is crucial to evaluate the rockburst risk during excavation of a deep tunnel by blasting. High *in-situ* stress inevitably endows high strain energy to the rock mass, which may be released in some forms by the rock mass after blasting excavation. Many studies have reported that the rockburst is a mechanical failure phenomenon caused by the energy release of the rock mass (Wang and Park, 2001; He et al., 2010; Su, et al., 2017; Su, et al., 2018; Chen, et al., 2019). Thus, the key to revealing the evolution mechanism of rockbursts is to explore the energy release regularities that result from blasting excavation of a deep-buried tunnel.

3 POST-PEAK MECHANICAL PROPERTY OF JINPING MARBLE AND ITS NUMERICAL DESCRIPTION

3.1 Post-peak Mechanical Property of Marble

Because rockbursts are the brittle failure induced behaviour of rock masses, the mechanical property, especially the post-peak mechanical characteristic of Jinping marble should be first studied to investigate the evolution mechanism of the rockburst that took place during the blasting excavation of No. 2 diversion tunnel. Previous research has reported that the stress-strain response and the yield form of the marble do not present as a single pattern under the action of compressive stress, but are closely associated with the value of confining pressure. For instance, in the case of low confining pressure, the stress-strain curve of the marble drops rapidly after reaching peak strength. This shows that the marble presents brittle characteristics like granite under low confining pressure. Accompanied with the continuous rise of confining pressure, it shows that the stress-strain curve slowly declines and the marble after the peak has a definite bearing capacity. While the confining pressure increases to a high level, the stress-strain curve of the marble after the peak does not decline and the residual strength of the marble still stays constant, presenting perfectly plastic characteristics. Therefore, the marble after the peak presents the brittle-ductile-plastic (BDP) transition characteristic during the rising process of confining pressure (Wawersik and Fairhurst, 1970). This particular mechanical property leads to the marble after the peak, which still has a high bearing capacity under the high confining pressure and stores a large amount of strain energy, which may be abruptly released and cause rockbursts under the disturbance of the tunnel excavation. Hence, studying and describing the BDP transition characteristics of Jinping marble is not only important for revealing the energy release regularities resulting from the transient stress unloading on the excavation boundary, but also are helpful for further understanding the evolution mechanism of the rockburst that happened during the construction of No. 2 diversion tunnel.

Aiming at investigating the special mechanical properties of Jinping marble, marble samples with a burial depth of 2000 m were drilled and obtained at the east end of the auxiliary tunnel for testing (Chu, 2009). Using the MTS pressure test equipment, a triaxial compression test was performed (see **Figure 4**). The test result in **Figure 4** indicates that the Jinping marble sample shows significantly brittle characteristics after reaching peak strength under low confining pressure (2 MPa). While the confining pressure rises to the level of 2~8 MPa, the residual strength of the marble sample drops a little and retains a high value after the peak. It shows that the marble sample starts presenting ductility features. As the confining pressure rises to a level of 40 MPa, the residual strength of the marble sample after the peak does not reduce and shows perfectly plastic characteristics.

3.2 Numerical Description Method of the Post-peak Mechanical Properties for Jinping Marble

To reveal the energy release regularity derived from the transient stress unloading during the tunnel excavation of the Jinping II hydropower project, first and foremost, the post-peak mechanical property of Jinping marble needs to be described. In the Hoek-Brown strength criterion, the mechanical parameters m_b, s, a, etc. can be changed with the increase of plastic strain ε_3^p after the material yielding. Therefore, the hardening and softening behaviour of Jinping marble after the peak can be described by the Hoek-Brown strength criterion. In this research, the Hoek-Brown strength criterion in FLAC3D was employed to simulate the brittle-ductility-plastic (BDP) transition characteristic of Jinping marble. The yield equation is (Cundall et al., 2003):

$$F_0 = \sigma_1 - \sigma_3 - \sigma_{ci}\left(m_b\frac{\sigma_3}{\sigma_1} + s\right)^a = 0 \tag{1}$$

here, m_b, s, and a are strength parameters relating to the quality evaluation of the rock mass *GSI*, the material parameters of the rock mass m_i; σ_1, σ_3, and σ_{ci} are the first principal stress, third principal stress, and uniaxial compressive strength of the material, respectively.

In the above strength criterion, the rule is assumed that the maximum plastic strain increment $\Delta\varepsilon_1^p$ and the minimum plastic strain increment $\Delta\varepsilon_3^p$ satisfy the following relationship:

$$\Delta\varepsilon_1^p = \gamma\Delta\varepsilon_3^p \tag{2}$$

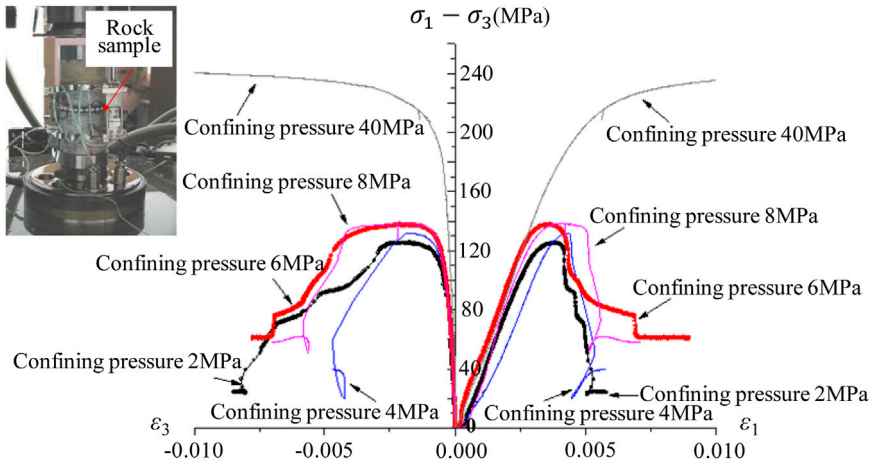

FIGURE 4 | Triaxial compression tests of Jinping T_{2b} marble samples.

here, γ is the factor associated with the stress level, and its value is updated in each calculation step with the increment of plastic strain. According to the yield stress level, four kinds of flow rules can be achieved by the Hoek-Brown strength criterion.

1) Associated flow rule

The rule for associated flow:

$$\Delta\varepsilon_i^p = -\gamma_{af}\frac{\partial F_0}{\partial\sigma_i} \tag{3}$$

Substituting **Eq. 1** and **Eq. 2** into **Eq. 3**, the associated flow factor γ_{af} can be obtained by the following formula:

$$\gamma_{af} = -\frac{1}{1 + am_b\left(m_b\frac{\sigma_3}{\sigma_1} + s\right)^{a-1}} \tag{4}$$

The associated flow rule is employed for the description of yield characteristics under the low confining pressure condition.

2) Isovolumetric flow rule

In the case of the higher confining pressure (σ_3^{cv}), the loading process will not terminate, and the volume of rock mass remains invariant in the subsequent loading process. Therefore, for the case of high confining pressure, this rule can describe the yield characteristic. The mathematical expression of this rule is:

$$\gamma_{if} = -1 \tag{5}$$

here, γ_{if} is the isovolumetric flow factor.

3) Radial flow rule

The rule is written by:

$$\gamma_{rf} = \frac{\sigma_1}{\sigma_3} \tag{6}$$

here, γ_{rf} is the radial flow factor.

The radial flow rule can describe the tensile failure of rock masses under the action of the tensile stress.

4) Combination flow rule

When the confining pressure ranges from 0 to σ_3^{cv}, the flow rule of the rock mass after yielding should be between the associated flow rule and the isovolumetric flow rule. Hence, a combination flow rule can be used to describe the yield characteristic:

$$\gamma_{cf} = \frac{1}{\frac{1}{\gamma_{af}} + \left(\frac{1}{\gamma_{if}} - \frac{1}{\gamma_{af}}\right)\frac{\sigma_3}{\sigma_3^{cv}}} \tag{7}$$

here, γ_{cf} is the combination flow factor.

Only the above four kinds of flow rules are still insufficient to describe the BDP transition characteristic of Jinping marble. To solve this issue, a scaling factor μ associated with the minimum principal stress σ_3 was proposed by Cundall et al. (2003) to simulate the softening and hardening characteristic of the rock mass after yielding. By adjusting the value of the factor μ, it can be used to describe the variation characteristic of the strength parameters m_b, s, a, etc. changing with the plastic strain under the different confining pressure conditions. Using the scaling factor μ, the brittle failure of granite was successfully described by Diederichs, on this basis, the "V-shape" failure was reproduced at the Canadian underground research laboratory (Diederichs, 2007). To describe the BDP transition characteristic of Jinping marble, the scaling factor μ and 8 parameters including 4 peak intensity parameters and 4 residual strength parameters should be first determined (Zhang et al., 2010). By triaxial compression test, the peak and residual strength parameters were acquired, which are given in **Table 2** and **Table 3**. As for the determination of scaling factor μ, in this paper,

TABLE 2 | Hoek-Brown mechanical parameters and *in-situ* stress field at K11+105 cross section.

Compressive strength	Elastic modulus	*GSI*	m_i	m_b	*s*	*a*
140 MPa	36.1 GPa	70	9	3.0827	0.0357	0.5
tensile strength	s_{xx}	s_{yy}	s_{zz}	s_{xy}	s_{xz}	s_{yz}
1.6 MPa	43.9 MPa	50.8 MPa	38.5 MPa	2.4 MPa	-3.0 MPa	3.6 MPa

TABLE 3 | Strength parameters of rock mass change with the plastic strain.

Case	Characteristic description	$\varepsilon_3^p/10^{-3}$	σ_{ci}/MPa	m_b	*s*	*a*
Condition one	Peak strength	0.00	140	3.0827	0.0357	0.50
	Ductility section	1.20	140	3.0827	0.0357	0.50
	Residual strength	2.30	140	4.1200	0	0.63
Condition two	Peak strength	0.00	140	3.0827	0.0357	0.50
	Ductility section	1.20	140	3.0827	0.0357	0.50
	Residual strength	2.30	140	3.6500	0	0.63

TABLE 4 | Scaling factor changes with the minimum principal stress.

Condition	σ_3/MPa	**0**	**2**	**4**	**8**	**12**	**15.9**	**16**
one	μ	1.00	0.75	0.65	0.55	0.45	0.35	0
Condition	σ_3/MPa	**0**	**2**	**4**	**8**	**18**	**24.9**	**25**
two	μ	1.00	0.85	0.75	0.65	0.45	0.34	0

the comparison method of the numerical simulation and the actual measured result of damage zones was adopted. For example, various conditions corresponding to different scaling factors μ were assumed, and then the *in-situ* stress unloading caused stress change path and damage zones of the surrounding rock mass were simulated using the assumed scaling factor μ. If the low stress distribution region and the extent of damage zones obtained by numerical simulation are consistent with the range of the low velocity distribution belt in the surrounding rock mass measured by the field acoustic wave test, it means that the right scaling factor μ has been found. Due to the troublesome process, here only two assumed conditions are introduced (**Table 4**).

Condition one: the rock mass presents the brittle characteristic at the low confining pressure (0–2 MPa). The mechanical property transition of ductile-plastic occurs with the confining pressure reaching the level of 16 MPa.

Condition two: the ductile-plastic transition happens when confining pressure reaches 25 MPa.

Adopting the parameters given in **Table 2**, **Table 3** and **Table 4**, taking the blasting excavation of No.2 diversion tunnel as an instance, the stress change path of the rock mass at a certain position of the surrounding rock mass under the disturbance of transient stress unloading on the excavation boundary was simulated, as shown in **Figure 5**. During the numerical modelling, the non-reflecting boundary condition was adopted, the stress dynamic adjustment processes of the rock mass elements which have a 30°angle with the *x*-axis (hole 4#) and have 1.0, 1.5, 2.0, 2.5, 3.0 m distance from the excavation boundary were recorded (**Figure 5**). In **Figure 5**, the fitting curve of peak strength and residual strength is also drawn. **Figure 5A** also presents that when the confining pressure reaches 16 MPa, the fitting curve of peak strength intersects the fitting curve of residual strength for condition one. It indicates that the confining pressure of the ductility-plastic transition is 16 MPa. While for condition two, the confining pressure of the ductility-plastic transition is 25 MPa (**Figure 5B**).

In **Figure 5**, when the stress path curve intersects the fitting curve of peak strength, it means that the rock mass element is damaged, and the larger falling of the stress path curve means there is worse damage to the surrounding rock mass. For condition one, the stress paths of the surrounding rock mass elements with the distances of 1.0 and 1.5 m from the excavation boundary both have a significant drop after reaching the fitting curve of peak strength, but the stress path of the surrounding rock mass element with 2.0 m distance from the excavation boundary does not fall. Therefore, the damage depth of the surrounding rock mass has a 30°angle with the *x*-axis (hole 4#) can be determined as 2.0 m. While for condition two, the stress path curve of the surrounding rock mass element with a distance of 2.0 m from the excavation boundary only has a slight drop after reaching the fitting curve of peak strength. The stress path curve of the surrounding rock mass element with a 2.5 m distance from the excavation boundary does not reach the fitting curve of peak strength, it means that the extent of damage to the surrounding rock mass is within 2.0~2.5 m. By further drawing the stress path curve of the rock mass element with a 2.0~2.5 m distance from the excavation boundary, it was found that the damage depth was 2.3 m at this location.

More simply, a square model (1 × 1 × 1 m) was set up to simulate the rock sample, and the numerical stress-strain curve in several confining pressure conditions was performed (**Figure 6**). As can be seen from **Figure 6**, the confining pressure plays a critical role in the mechanical characteristic of the marble after the peak.

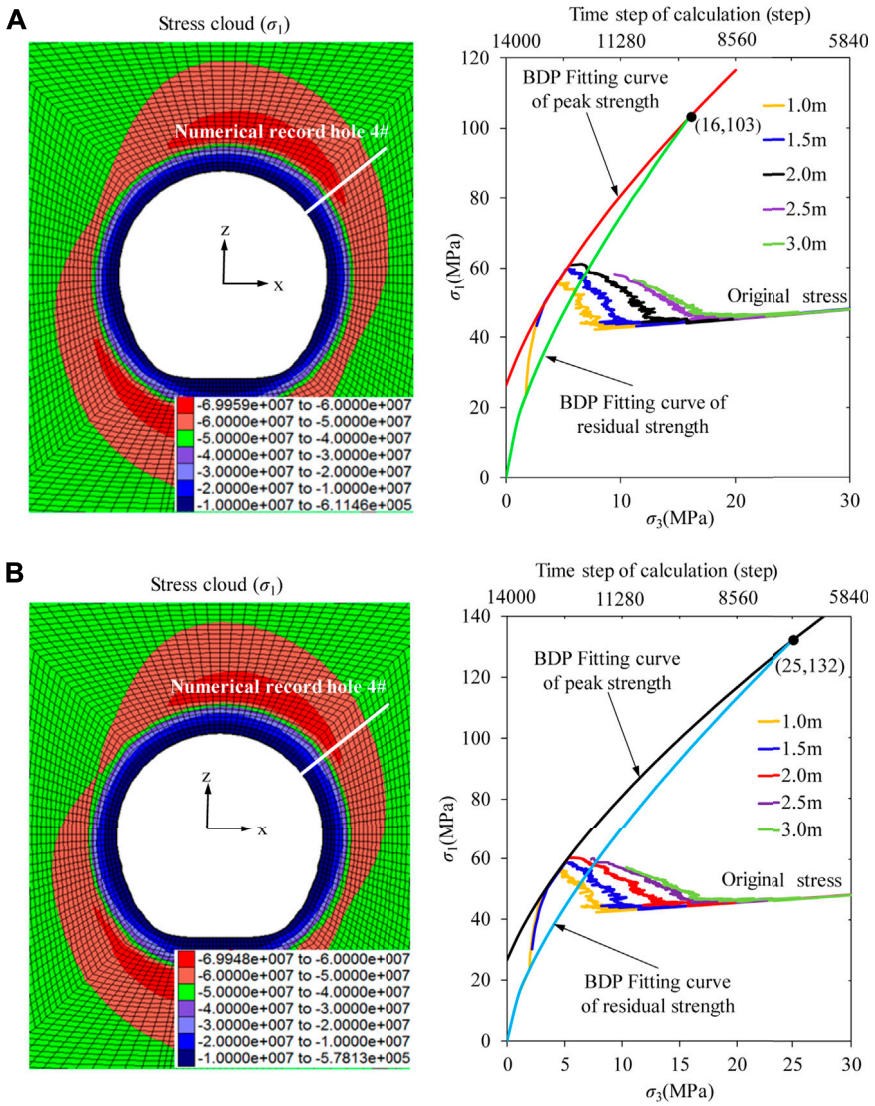

FIGURE 5 | Stress path of surrounding rock masses induced by excavation. **(A)** Condition one, **(B)** Condition two.

When the confining pressure is low (0~2 MPa), the stress-strain curve falls quickly after the peak and presents the obviously brittle characteristic like granite, and there is still a significant difference between the peak strength and the residual strength. However, this difference continually declines with the rise of the confining pressure. While the confining pressure exceeds 10 MPa, the stress-strain curve does not fall quickly after yielding and shows a significantly ductile characteristic. When the numerical rock sample is under high confining pressure, the stress-strain curve does not decline after the peak and shows an ideally plastic characteristic. For condition one, the confining pressure 16 MPa is the ductility-plastic transition threshold. While for condition two, the confining pressure 25 MPa is the ductility-plastic transition threshold. Both conditions one and two can describe the BDP transition property of the marble. To deduce which condition is right, a verification using the field acoustic wave test needs to be performed.

The field acoustic wave test result of the cross-section K11+105 is given in **Figure 7**. From **Figure 7**, the damage depth of the surrounding rock mass which has a 30°angle with the *x*-axis (hole 4#) is 2.0 m. It can be found that the test result is consistent with the numerical simulation result of condition one in **Figure 5A**. On this basis, using the parameters of condition one, the damage zone of the surrounding rock mass resulting from tunnel excavation was simulated (see **Figure 7**). In **Figure 7**, we can find that except for hole 2#, there is little difference between the damage extent of simulation results and the damage extent of field test results, which proves that the simulation method adopted in this paper is correct. Because the indoor test presented in **Figure 4** is hard to reproduce the real loading and unloading stress path of the surrounding rock mass, it may lead to the numerical axial stress-strain curves in **Figure 6** being inaccurate. This is why the axial stress-strain curves of simulation results in **Figure 6** are different from that of

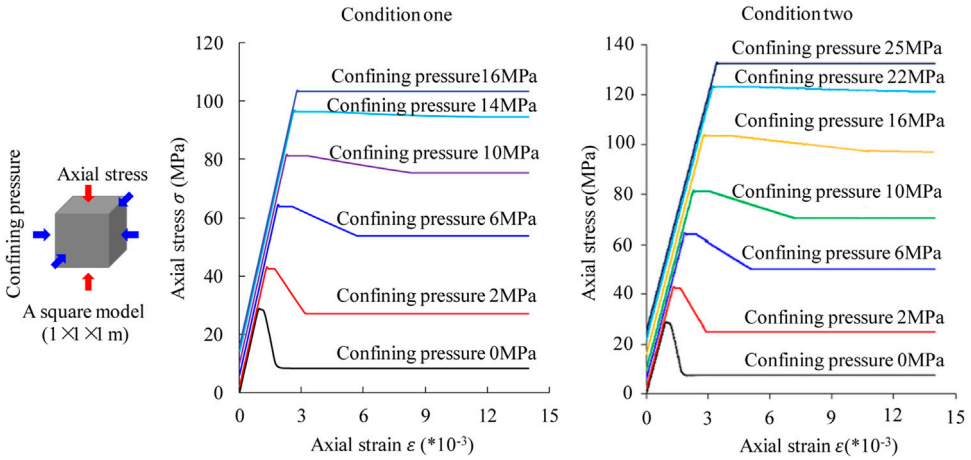

FIGURE 6 | Axial stress-strain curves under different conditions.

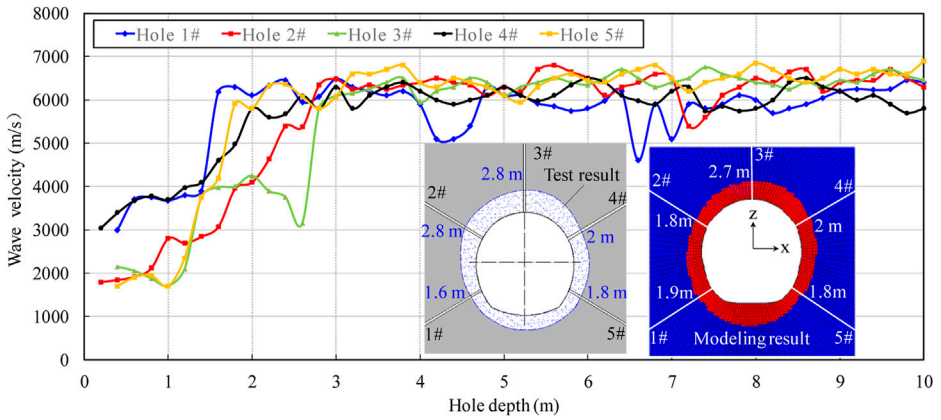

FIGURE 7 | Field test results of acoustic wave and excavation induced damage zone at K11+105 cross section.

indoor test results in **Figure 4**, but the simulation result of the damage zone is the same as the field test result.

4 ENERGY VARIATION AND RELEASE PROCESS OF THE SURROUNDING ROCK MASS AROSE FROM STRESS UNLOADING

4.1 Energy Accumulation Process of the Surrounding Rock Mass and Its Energy Storage Limit

A simple assumption was made that an infinite-long tunnel is excavated with a radius of R in the initial hydrostatic stress field P_0. Then, the stress adjustment process of the surrounding rock mass due to the quasi-static unloading of *in-situ* stress can be calculated by **Eq. 8**:

$$\left.\begin{aligned}\sigma_1 &= \sigma_\theta = P_0\left(1+\frac{R^2}{r^2}\right)\\ \sigma_2 &= P_0\\ \sigma_3 &= \sigma_r = P_0\left(1-\frac{R^2}{r^2}\right)\end{aligned}\right\} \tag{8}$$

here, r is the distance between the rock mass and the excavation centre, σ_θ and σ_r are the circumferential stress and radial stress, respectively, and σ_1, σ_2, σ_3 are the principal stresses.

After the calculation of principal stresses, the density of elastic strain energy can be counted by **Eq. 9** (Solecki and Conant, 2003):

$$U = \frac{\left[\sigma_1^2+\sigma_2^2+\sigma_3^2-2\upsilon(\sigma_1\sigma_2+\sigma_2\sigma_3+\sigma_1\sigma_3)\right]}{2E_0} \tag{9}$$

here, υ is the Poisson's ratio, E_0 is the elastic modulus, and U is the elastic strain energy density of the rock mass at a certain location.

Before tunnel excavation (σ_1=σ_2=σ_3=P_0), the initial rock mass is intact and its strain energy density is counted by:

$$U_0 = \frac{(3-6\upsilon)P_0^2}{2E_0} \tag{10}$$

here, U_0 is the initial strain energy density of rock masses before the tunnel excavation.

When the unloading process is completed, the strain energy density of the surrounding rock mass can be obtained by substituting **Eq. 8** into **Eq. 9**:

$$U_A = \frac{P_0^2\left[3-6\upsilon+2(1+\upsilon)\frac{R^4}{r^4}\right]}{2E_0} \tag{11}$$

here, U_A is the strain energy density of the surrounding rock mass at a certain position after stress unloading.

Comparing **Eq. 10** and **Eq. 11**, it is not difficult to find that after the *in-situ* stress unloading induced by tunnel excavation, the strain energy density of the surrounding rock mass increases.

It is generally acknowledged that as a brittle material, there is a limit for the strain energy storage capacity of the rock mass. Based on the hydrostatic compressive pressure field considered in this research, the energy storage limit of the rock mass U_c for the case of three-dimensional pressure can be calculated by **Eq. 12** (Xie et al., 2005):

$$U_c = \frac{\sigma_c^3}{2E_0(\sigma_1-\sigma_3)} \tag{12}$$

Under the condition of the quasi-static unloading, U_c is acquired by substituting **Eq. 8** into **Eq. 12**:

$$U_c = \frac{r^2\sigma_c^3}{4R^2E_0P_0} \tag{13}$$

From **Eq. 13** and **Eq. 11**, it can be found that the shorter distance to the excavation centre, the weaker the energy storage capacity of the rock mass, and the more the strain energy will accumulate in the rock mass. Consequently, when it is close to the excavation boundary, the strain energy aggregated in the surrounding rock mass can easily exceed the storage limit, which will inevitably lead to the energy release and cause damage, even failure in the surrounding rock mass.

When the blasting excavation method is employed, the stress unloading process on the excavation face is rapid and transient but not a quasi-static process (Lu et al., 2012; Li et al., 2014; Zhu et al., 2014; Fan et al., 2015). The transient stress unloading induced stress field in the surrounding rock mass can be calculated by employing inversion integral, contour integration, and Laplace transform (Fan et al., 2016):

$$\frac{\sigma_r(r,t)}{P_0} = \begin{cases} 1 & \Rightarrow\left(t<\frac{(r-R)}{C_p}\right) \\ 1-\frac{R^2}{2t_0r^2}\left(t-\frac{(r-R)}{C_p}\right)-\frac{1}{\pi t_0}\int_0^{\infty}Q_1(\eta,t)d\eta & \Rightarrow\left(\frac{(r-R)}{C_p}\le t\le\frac{(r-R)}{C_p+t_0}\right) \\ 1-\frac{R^2}{2r^2}-\frac{1}{\pi t_0}\int_0^{\infty}Q_2(\eta,t)d\eta & \Rightarrow\left(t>\frac{(r-R)}{C_p+t_0}\right) \end{cases} \tag{14}$$

$$\frac{\sigma_\theta(r,t)}{P_0} = \begin{cases} 1 & \Rightarrow\left(t<\frac{(r-R)}{C_p}\right) \\ 1+\frac{R^2}{2t_0r^2}\left(t-\frac{(r-R)}{C_p}\right)-\frac{1}{t_0\pi}\int_0^{\infty}Q_3(\eta,t)d\eta & \Rightarrow\left(\frac{(r-R)}{C_p}\le t\le\frac{(r-R)}{C_p+t_0}\right) \\ 1+\frac{R^2}{2r^2}-\frac{1}{t_0\pi}\int_0^{\infty}Q_4(\eta,t)d\eta & \Rightarrow\left(t>\frac{(r-R)}{C_p+t_0}\right) \end{cases} \tag{15}$$

here:

$$Q_1 = \frac{(A_r+B_r)\left[\cos\left(\frac{(r-R)}{C_p}\eta\right)-\cos(t\eta)\right]}{(E+F)\eta^2} + \frac{(C_r-D_r)\left[\sin(t\eta)-\sin\left(\frac{(r-R)}{C_p}\eta\right)\right]}{(E+F)\eta^2}$$

$$Q_2 = \frac{(A_r+B_r)\left[\cos((t-t_0)\eta)-\cos(t\eta)\right]}{(E+F)\eta^2} + \frac{(C_r-D_r)\left[\sin(t\eta)-\sin((t-t_0)\eta)\right]}{(E+F)\eta^2}$$

$$Q_3 = \frac{(A_\theta+B_\theta)\left[\cos(t\eta)-\cos\left(\frac{(r-R)}{C_p}\eta\right)\right]}{(E+F)\eta^2} + \frac{(C_\theta-D_\theta)\left[\sin(t\eta)-\sin\left(\frac{(r-R)}{C_p}\eta\right)\right]}{(E+F)\eta^2}$$

$$Q_4 = \frac{(A_\theta+B_\theta)\left[\cos(t\eta)-\cos((t-t_0)\eta)\right]}{(E+F)\eta^2} + \frac{(C_\theta-D_\theta)\left[\sin(t\eta)-\sin((t-t_0)\eta)\right]}{(E+F)\eta^2}$$

$$A_r=\alpha_1\alpha_2, B_r=\alpha_3\alpha_4, C_r=\alpha_1\alpha_4, D_r=\alpha_2\alpha_3, E=\alpha_2^2, F=\alpha_4^2,$$
$$A_\theta=\alpha_5\alpha_2, B_\theta=\alpha_6\alpha_4, C_\theta=\alpha_5\alpha_4, D_\theta=\alpha_2\alpha_6$$

$$\alpha_1=\left(\frac{2}{G^2r}J_1-\frac{\eta}{C_p}J_0\right)\left(\frac{\eta}{C_p}r\right), \alpha_2=\left(\frac{2}{G^2R}J_1-\frac{\eta}{C_p}J_0\right)\left(\frac{\eta}{C_p}R\right)$$

$$\alpha_3=\left(\frac{2}{G^2r}Y_1-\frac{\eta}{C_p}Y_0\right)\left(\frac{\eta}{C_p}r\right), \alpha_4=\left(\frac{2}{G^2R}Y_1-\frac{\eta}{C_p}Y_0\right)\left(\frac{\eta}{C_p}R\right)$$

$$\alpha_5=\left(-\frac{2}{G^2r}J_1-\left(1-\frac{2}{G^2}\right)\frac{\eta}{C_p}J_0\right)\left(\frac{\eta}{C_p}r\right),$$
$$\alpha_6=\left(-\frac{2}{G^2r}Y_1-\left(1-\frac{2}{G^2}\right)\frac{\eta}{C_p}Y_0\right)\left(\frac{\eta}{C_p}r\right)$$

here, C_p is the P-waves velocity, t and t_0 is the time and unloading time, respectively, $\sigma_\theta(r, t)$ and $\sigma_r(r, t)$ is the dynamically circumferential stress and radial stress of the surrounding rock mass induced by transient unloading, respectively, η is the integral path, G is the Lame constant, J_0, J_1, Y_0, and Y_1 are the Bessel functions.

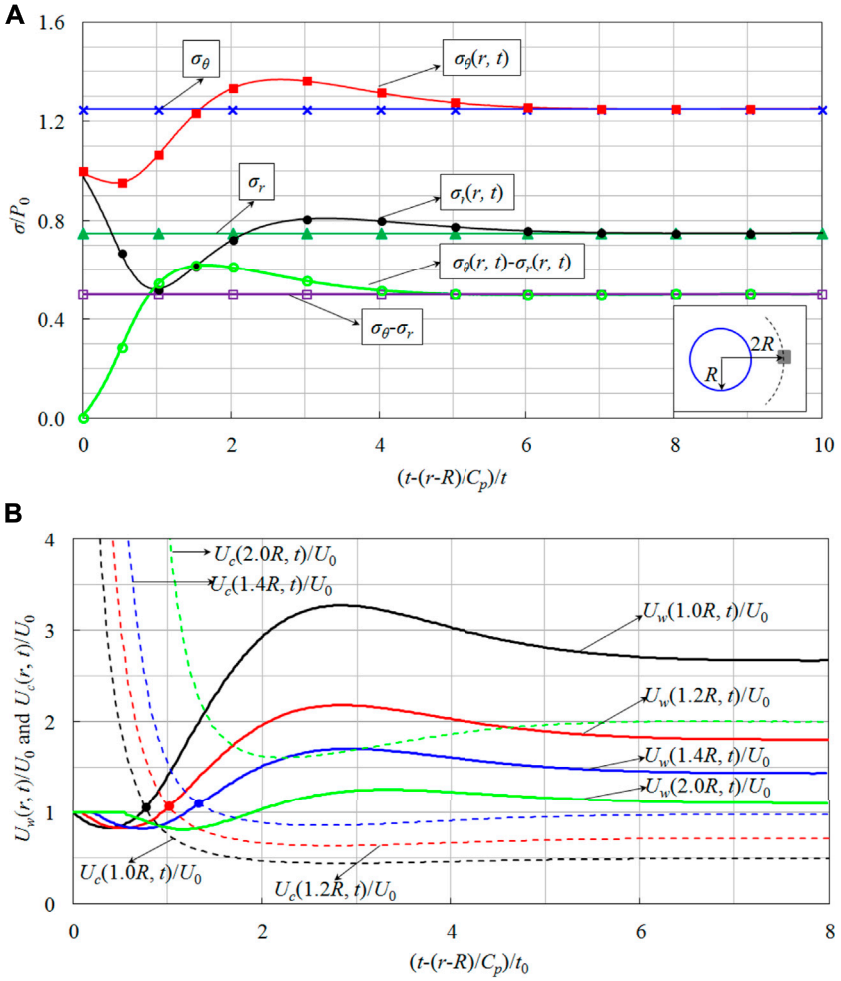

FIGURE 8 | Dynamic response induced by transient unloading of *in-situ* stress. **(A)** Dynamic stress of surrounding rock masses induced by transient unloading of *in-situ* stress ($r = 2R$), **(B)** Variation process of strain energy density and energy storage limit induced by transient unloading of *in-situ* stress.

After calculation, the dynamically circumferential stress and radial stress of the surrounding rock mass are drawn in **Figure 8A**. From **Figure 8A**, compared with quasi-static unloading, transient unloading will enlarge the effect of radial unloading and circumferential loading in the surrounding rock mass, and result in a larger difference between the first and third principal stress. Combining this dynamic adjustment process with **Eq. 12**, the transient stress unloading will reduce the energy storage limit and tends to result in energy release.

Substituting the dynamic stress field of **Figure 8A** into **Eq. 9**, the strain energy density of the surrounding rock mass $U_w(r, t)$ under the transient stress unloading can be calculated. To show the variation process of strain energy intuitively, the ratios of the strain energy density $U_w(r, t)$ and energy storage limit $U_c(r, t)$ to the initial strain energy density U_0 of the surrounding rock mass at $1.0R$, $1.2R$, $1.4R$, and $2.0R$ are drawn in **Figure 8B**. As can be seen from **Figure 8B**, the strain energy experiences a dynamic variation process like declining at first, raising second and stabilizing at last. In fact, before the strain energy reaches the peak value of the elastic change curve as shown in **Figure 8B**, it will exceed the energy storage limit and result in energy release. Obviously, under elastic conditions, the subsequent curve after the strain energy density curve intersecting with the energy storage limit curve is not the actual energy adjustment process.

4.2 Description Indicators of Energy Release

On the purpose of evaluating the rockburst intensity, Cook proposed a new index, energy release rate (*ERR*), which can be counted by **Eq. 16**:

$$ERR = \frac{(E_s + E_e)}{V_e} \tag{16}$$

here, E_s is the total value of released energy; E_e and V_e are the total strain energy and volume of the excavated rock mass, respectively.

Since the energy release rate (*ERR*) cannot reflect the intensity and location of the energy release in the

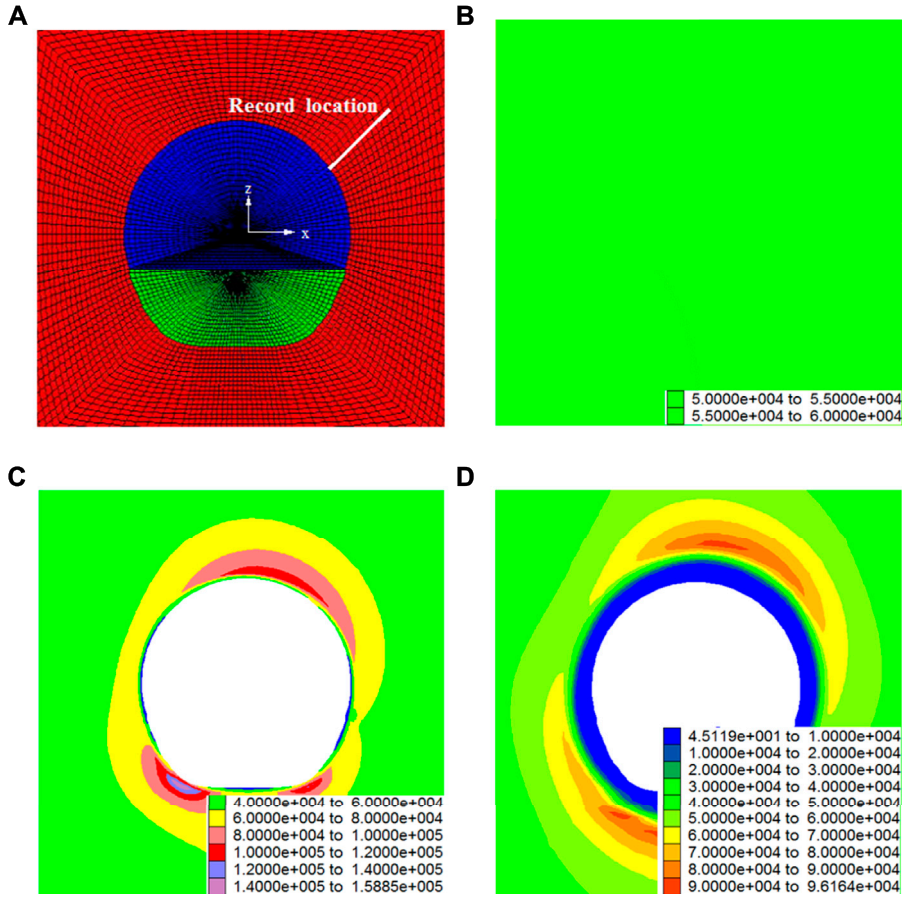

FIGURE 9 | The variation of strain energy due to tunnel excavation (J/m^3): **(A)** Calculation model, **(B)** Strain energy of initial rock masses before excavation, **(C)** Strain energy accumulation in surrounding rock masses, **(D)** residual state of strain energy in surrounding rock masses.

surrounding rock mass, it fails to identify the occurrence position of the rockburst. To achieve this goal, an index of local energy release rate (*LERR*) was proposed by Jiang et al. (2010) for describing the energy release resulting from the tunnel excavation. This index is acquired by counting the difference value between the strain energy density before the material failure and the strain energy density after the material failure:

$$LERR_i = U_{ipeak} - U_{itrough} \tag{17}$$

here, $LERR_i$ is *LERR* of the rock mass element; U_{ipeak} is the peak value of strain energy density of the rock mass element before the brittle failure; $U_{itrough}$ is the trough value of strain energy density of the rock mass element after the brittle failure; i is the number of the rock mass element; U_{ipeak} and $U_{itrough}$ are counted by **Eq. 9**.

From **Figure 8B**, it can also be seen that the residual value of strain energy density may be higher than the trough value of strain energy density under the elastic condition after the brittle failure occurring. Therefore, **Eq. 17** should be corrected:

$$LERR_i = U_{i\max} - U_{is} \tag{18}$$

here, U_{imax} is the maximum value of strain energy density for the i-th rock mass element before the brittle failure happens; U_{is} is the final stable value or the residual value of strain energy density after the brittle failure.

4.3 Numerical Simulation

The same model (**Figure 9A**) and parameters in **section 3.2** were adopted to analyze the energy release process due to excavation. Before excavation, adopting the ideal and elastic model, the initial *in-situ* stress field and strain energy of rock masses was calculated. Through a certain calculation time step, the balance was obtained and the simulation result is shown in **Figure 9B**. During the numerical simulation of the energy release process, the non-reflecting boundary condition, i.e. the energy absorption boundary condition mentioned in **Section 3.2** was adopted. Then, based on the parameters in **Table 2**, **Table 3**, and **Table 4** and the BDP model, the energy accumulation of the surrounding rock mass due to tunnel excavation was simulated as shown in **Figure 9C**. From the simulation result presented in **Figure 9C**, it was found that due to the low storage limit of the surrounding rock mass around the excavation

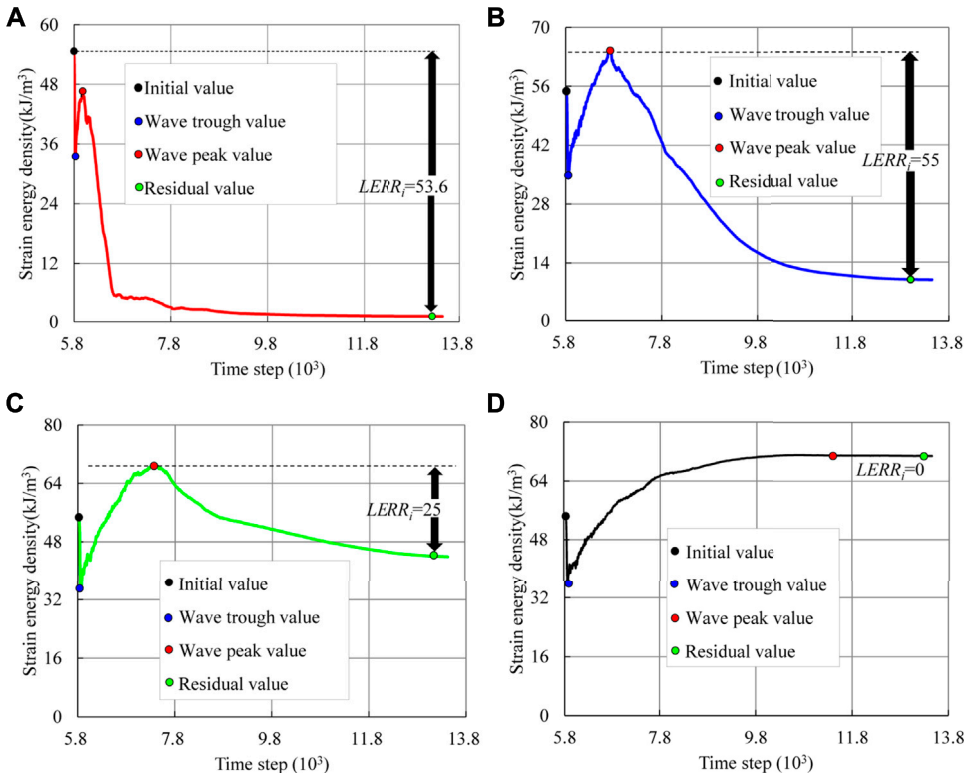

FIGURE 10 | Energy release process of surrounding rock masses induced by the transient unloading of *in-situ* stress: **(A)** Rock mass element with a distance of 0.5 m from the excavation boundary, **(B)** Rock mass element with a distance of 1.0 m from the excavation boundary, **(C)** Rock mass element with a distance of 1.5 m from the excavation boundary, **(D)** Rock mass element with a distance of 2.0 m from the excavation boundary.

boundary, the accumulated strain energy easily exceeds the energy storage limit. Subsequently, energy release happens and triggers off the failure of the surrounding rock mass. After the energy release process is complete, the strain energy stabilizes at the residual state, as in **Figure 9D**.

To reveal the dynamic process of energy release resulting from transient stress unloading, the strain energy density of the surrounding rock mass elements with the distances of 0.5, 1.0, 1.5, and 2.0 m from the excavation boundary (**Figure 9A**) were recorded, which is drawn in **Figure 10**.

Figure 10 shows that the strain energy adjustment curve has two significant amplitude values: the peak value and the trough value. For the rock mass element which is 0.5 m away from the excavation boundary (**Figure 10A**), the peak value of the strain energy density is smaller than its initial value. While for the rock mass element with distances of 1.0 and 1.5 m from the excavation boundary, the peak value of the strain energy density is greater than the initial value (see **Figures 10B,C**). This illustrates that due to transient stress unloading, the strain energy of the distant rock mass will flow to the excavation boundary and lead to the accumulated energy more easily exceeding the energy storage limit for the rock mass, which is near the excavation boundary. Thus, when the strain energy accumulates in the surrounding rock mass, it cannot reach the peak value like **Figure 8B** under the ideally elastic conditions, it can even be smaller than the initial value of the strain energy before excavation unloading. Therefore, it is inaccurate to use the difference value of the peak value and trough value (**Eq. 17**) when calculating the local energy release rate.

Figure 10 indicates that for the surrounding rock mass elements which are 0.5, 1.0, and 1.5 m away from the excavation boundary, the strain energy experiences a variation process of reducing firstly, raising secondly, then decreasing and finally stabilizing. Similar to the elastic conditions, the first reduction of strain energy will not trigger failures in the surrounding rock mass, because it is induced by the elastic unloading wave. However, the second decline of the strain energy results from the factor that the strain energy absorbed in the surrounding rock mass, which is greater than the storage limit, which will inevitably lead to the brittle failure of the surrounding rock mass. A further observation from **Figure 10**, it is not difficult to find that with the decrease of the distance between the rock mass and the excavation boundary, the energy release duration is shorter, and the local energy release rate is greater. These characteristics mean that the shorter distance from the rock mass to the final excavation boundary, the more violent energy release occurs.

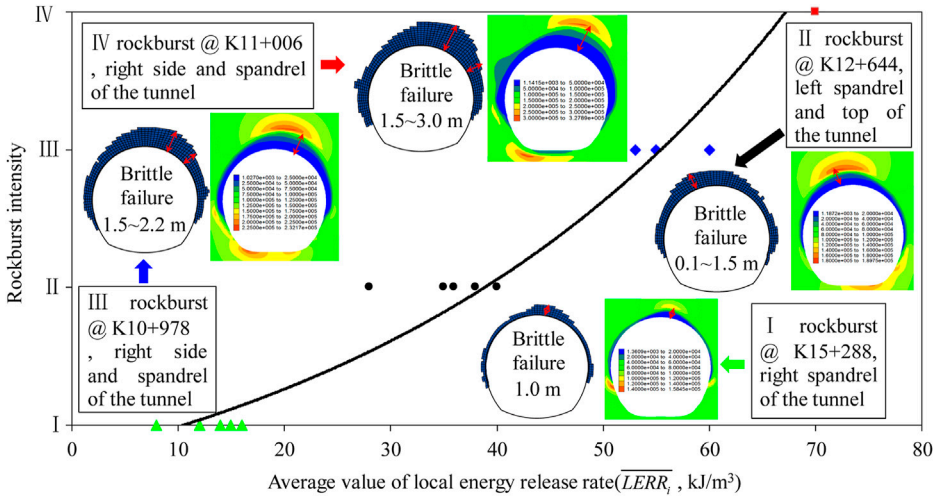

FIGURE 11 | Relationship between the average value of local energy release rate ($\overline{LERR_i}$) and rockburst intensity.

4.4 Relationship Between Energy Release and Rockburst Intensity

For the deep tunnel excavation, the energy release is the inherent factor of the dynamic failure of the surrounding rock mass such as rockbursts (Hodgson and Joughin, 1966; Toksöz and Kehrer, 1972; Singh, 1988; Mikhalyuk and Zakharov, 1997; Wang and Park, 2001; He et al., 2010). Therefore, establishing a certain association of the energy release and the rockburst is crucial to predicting and controling the rockburst induced by the deep tunnel excavation. Based on the concept of *LERR*, the average value of the local energy release rate $\overline{LERR_i}$ is proposed, which can be written by:

$$\overline{LERR_i} = \frac{\sum_{i}^{n} LERR_i}{V_f} \tag{19}$$

here, V_f is the total volume of the failure *elements* in surrounding rock masses.

Based on the recorded rockbursts in **Table 1**, the average value of $\overline{LERR_i}$ was calculated. Afterwards, the relationship between the average value of $\overline{LERR_i}$ and rockburst intensity was set up as shown in **Figure 11**. Then, using the mechanical parameters in **Table 2**, **Table 3**, and **Table 4** and the *in-situ* stress fields in **Figure 1C**, the failure extent and final energy distribution of the surrounding rock mass for different rockburst grades at several stake numbers were simulated (**Figure 11**), and the comparison of between the numerical simulation and the measured result for the stake number K11+006 (rockburst grade IV), 10+978 (rockburst grade III), 12+644 (rockburst grade II), and 15+288 (rockburst grade I) is given in **Figure 11**. From **Figure 11**, the simulation extent of the brittle failure is consistent with the crater depth of the rockburst that occurred at the same stake number in **Table 1**. The simulation location of the brittle failure is consistent with the rockburst occurrence location at the tunnel cross-section in **Table 1**. For instance, the simulation extent of the brittle failure at stake number K11+006 is 1.5~3.0 m, mainly at the right side and spandrel. Similarly, the field observed rockburst at K11+006 has the same characteristic. This proves the accuracy of the numerical method employed in this paper.

Using the numerical simulation method proposed above, the average value of $\overline{LERR_i}$ was acquired. Then, the rockburst intensity can be predicted by the relationship curve in **Figure 11**. In addition, the residual state of strain energy was also simulated and drawn in **Figure 11** in the form of a cloud chart to determine the location of the rockburst. After the energy release, the lowest residual value of the strain energy means the largest energy release rate and the most drastic rockburst occurred in the surrounding rock mass. Therefore, both the intensity and location of the rockburst can be predicted by employing the relationship curve in **Figure 11** and the cloud chart of the residual strain energy.

The rockburst prediction is challenging work for researchers and engineers. Since the energy release plays a significant role in the formation of the rockburst, it has been the subject of much attention. The association between the rockburst intensity and the energy release rate (*ERR*) was developed by South African researchers, which can be expressed as:

$$ERR = \begin{cases} 16 \sim 34 & \Rightarrow \text{Slight rockburst (I)} \\ 34 \sim 53 & \Rightarrow \text{Medium rockburst (II)} \\ 53 \sim 100 & \Rightarrow \text{Intense rockburst (III)} \\ 100 \sim 140 & \Rightarrow \text{Drastic rockburst (IV)} \end{cases} \left(MJ/m^3\right) \tag{20}$$

The magnitude in **Eq. 20** is significantly different from that in **Figure 11**. Considering a simple case, under the burial depth of 1,000~2000 m, an underground tunnel is excavated with the *in-situ* stress of 27~54 MPa (assumption: υ=0.25, E_0=20~50 GPa). On this basis, the initial strain energy density of the rock mass can be estimated by **Eq. 10**. After calculation, the initial strain

energy density of the surrounding rock mass only reaches 10.9–109.4 kJ/m^3, which is similar to the magnitude in **Figure 11**. From this point of view, the prediction method of rockbursts proposed in **Figure 11** is better than that in **Eq. 20**.

The fault, structural plane, and excavation method were not considered in this paper but they also play a key role in the energy release and rockburst characteristics. Thus, the prediction method proposed for the rockburst (**Figure 11**) still requires verification. Despite these limitations, this research provides new insights to reveal energy variation regularity and assess the rockburst risk during the excavation of the deep tunnel by blasting.

5 CONCLUSION

Considering the special post-peak mechanical property of Jinping marble, the BDP transition property of Jinping marble was numerically simulated. Using the correct BDP model after verifications, we analyzed the transient stress unloading induced by the dynamic energy release process. Due to the transient unloading, the strain energy of the surrounding rock mass goes through a process of firstly decreasing, secondly increasing, next reducing, and finally stabilizing. Similar to the elastic conditions, the first decrease of strain energy results from the elastic unloading wave, which will not trigger the energy release and brittle failure. The second reduction of strain energy is owed to the factor that a quantity of strain energy accumulates in the surrounding rock mass and exceeds the storage limit of the surrounding rock mass, which inevitably causes the energy release and brittle failure of the surrounding rock mass. According to the theoretical calculation and numerical calculation, the shorter distance from the surrounding rock mass to the final excavation boundary means that the energy storage capacity of the surrounding rock mass is weaker, the intenser energy release, and the more drastic rockburst. Finally, to investigate the association of the energy release and rockburst due to the tunnel excavation, a numerical relationship between the average value of $LE\bar{R}R_i$ and the rockburst intensity was established to assess the rockburst risk induced by blasting excavation of the deep tunnel.

This research only reveals the dynamic energy release process derived from transient stress unloading and established the relationship between the average value of $LE\bar{R}R_i$ as well as the rockburst intensity for the rockburst prediction. Complex conditions such as structural planes and excavation methods were not considered. Therefore, further studies on the verification of the rockburst prediction method proposed in this paper under more complete working conditions will be performed in future work.

DATA AVAILABILITY STATEMENT

The raw data supporting the conclusions of this article will be made available by the authors, without undue reservation.

AUTHOR CONTRIBUTIONS

XC, ZL, JZ, FW, and XX contributed to the writing of the manuscript. YF led the field work. All authors contributed to giving constructive reviews and suggestions.

FUNDING

This work was supported by the National Natural Science Foundation of China (51979152), Educational Commission of Hubei Province of China (T2020005), Open Foundation of Hydraulic Rock Mechanics of Ministry of Education (RMHSE1603), Open Foundation of Hubei Key Laboratory of Construction and Management in Hydropower Engineering (2016KSD11).

ACKNOWLEDGMENTS

The authors would like to thank all the supporters.

REFERENCES

Alija, S., Torrijo, F. J., and Quinta-Ferreira, M. (2013). Geological Engineering Problems Associated With Tunnel Construction in Karst Rock Masses: the Case of Gavarres Tunnel (Spain). *Eng. Geology.* 157 (4), 103–111. doi:10.1016/j.enggeo.2013.02.010

Alija, S., Torrijo, F. J., and Quinta-Ferreira, M. (2014). Study of the Unexpected Collapse of the Ampurdán Tunnel (Spain) Using a Finite Elements Model. *Bull. Eng. Geol. Environ.* 73 (2), 451–463. doi:10.1007/s10064-013-0534-z

Brady, B. H. G., and Brown, E. T. (1981). Energy Changes and Stability in Underground Mining: Design Applications of Boundary Element Methods. *Inst. Mining Metall. Trans.* 90, 61–68.

Chen, Z., Su, G., Ju, J. W., Jiang, J., and Jiang, J. Q. (2019). Experimental Study on Energy Dissipation of Fragments during Rockburst. *Bull. Eng. Geol. Environ.* 78 (5), 5369–5386. doi:10.1007/s10064-019-01463-9

Chu, W. J. (2009). *Stability and Structure Safety Assessment of Surrounding Rock in Deep Buried Tunnel*. Hangzhou, China: Postdoctoral research report of Hydro China Huadong Engineering Corporation.

Cook, N. G. W., Hoek, E., Pretorius, J. P. G., Ortlepp, W. D., and Salamon, M. D. G. (1966). Rock Mechanics Applied to the Study of Rockbursts. *J. South Afr. Inst. Mining Metall.* 66 (10), 436–528.

Cook, N. G. W. (1976). Seismicity Associated With Mining. *Eng. Geology.* 10 (2), 99–122. doi:10.1016/0013-7952(76)90015-6

Cundall, P., Carranza-Torres, C., and Hart, R. (2003). "A New Constitutive Model Based on the Hoek–Brown Criterion," in Proceedings of the 3rd international FLAC symposium. Editor R Brummer (Sudbury: Balkema), 17–25.

Diederichs, M. S. (2007). The 2003 Canadian Geotechnical Colloquium: Mechanistic Interpretation and Practical Application of Damage and Spalling Prediction Criteria for Deep Tunnelling. *Can. Geotech. J.* 44 (9), 1082–1116. doi:10.1139/T07-033

Fan, Y., Lu, W. B., Yan, P., Chen, M., and Zhang, Y. Z. (2015). Transient Characters of Energy Changes Induced by Blasting Excavation of Deep-Buried Tunnels. *Tunnelling Underground Space Technology.* 49, 9–17. doi:10.1016/j.tust.2015.04.003

Fan, Y., Lu, W., Zhou, Y., Yan, P., Leng, Z., and Chen, M. (2016). Influence of Tunneling Methods on the Strainburst Characteristics During the Excavation

of Deep Rock Masses. *Eng. Geology.* 201, 85–95. doi:10.1016/j.enggeo.2015.12.015

Fan, Y., Zheng, J. W., Cui, X. Z., Leng, Z. D., Wang, F., and Lv, C. C. (2021). Damage Zones Induced by *In Situ* Stress Unloading During Excavation of Diversion Tunnels for the Jinping II Hydropower Project. *Bull. Eng. Geol. Environ.* 80 (8), 4689–4715. doi:10.1007/s10064-021-02172-y

Feng, X.-T., Xu, H., Qiu, S.-L., Li, S.-J., Yang, C.-X., Guo, H.-S., et al. (2018a). *In Situ* Observation of Rock Spalling in the Deep Tunnels of the China Jinping Underground Laboratory (2400 M Depth). *Rock Mech. Rock Eng.* 51 (4), 1193–1213. doi:10.1007/s00603-017-1387-8

Feng, X.-T., Guo, H.-S., Yang, C.-X., and Li, S.-J. (2018b). *In Situ* Observation and Evaluation of Zonal Disintegration Affected by Existing Fractures in Deep Hard Rock Tunneling. *Eng. Geology.* 242, 1–11. doi:10.1016/j.enggeo.2018.05.019

He, M. C., Miao, J. L., and Feng, J. L. (2010). Rock Burst Process of limestone and its Acoustic Emission Characteristics Under True-Triaxial Unloading Conditions. *Int. J. Rock Mech. Mining Sci.* 47 (2), 286–298. doi:10.1016/j.ijrmms.2009.09.003

Hodgson, K., and Joughin, J. C. (1966). The Relationship Between Energy Release Rate, Damage, and Seismicity in Deep Mines, *The 8th U.S. Symposium on Rock Mechanics (USRMS)*, Minneapolis, Minnesota: Johannesburg.

Jiang, Q., Feng, X.-T., Xiang, T.-B., and Su, G.-S. (2010). Rockburst Characteristics and Numerical Simulation Based on a New Energy index: a Case Study of a Tunnel at 2,500 M Depth. *Bull. Eng. Geol. Environ.* 69 (3), 381–388. doi:10.1007/s10064-010-0275-1

Kisslinger, C. (1976). A Review of Theories of Mechanisms of Induced Seismicity. *Eng. Geology.* 10, 85–98. doi:10.1016/0148-9062(77)90067-5

Kramarenko, V. I., and Revuzhenko, A. F. (1988). Flow of Energy in a Deformed Medium. *Soviet Mining Sci.* 24 (6), 536–540. doi:10.1007/BF02498611

Li, X., Cao, W., Zhou, Z., and Zou, Y. (2014). Influence of Stress Path on Excavation Unloading Response. *Tunnelling Underground Space Technology.* 42, 237–246. doi:10.1016/j.tust.2014.03.002

Lindin, G. L., and Lobanova, T. V. (2013). Energy Sources of Rockbursts. *J. Min Sci.* 49 (1), 36–43. doi:10.1134/S106273914901005X

Lu, W., Yang, J., Yan, P., Chen, M., Zhou, C., Luo, Y., et al. (2012). Dynamic Response of Rock Mass Induced by the Transient Release of *In-Situ* Stress. *Int. J. Rock Mech. Mining Sci.* 53 (7), 129–141. doi:10.1016/j.ijrmms.2012.05.001

Martino, J. B., and Chandler, N. A. (2004). Excavation-Induced Damage Studies at the Underground Research Laboratory. *Int. J. Rock Mech. Mining Sci.* 41 (8), 1413–1426. doi:10.1016/j.ijrmms.2004.09.010

Mikhalyuk, A. V., and Zakharov, V. V. (1997). Dissipation of Dynamic-Loading Energy in Quasi-Elastic Deformation Processes in Rocks. *J. Appl. Mech. Tech. Phys.* 38 (2), 312–318. doi:10.1007/BF02467918

Mitri, H. S., Tang, B., and Simon, R. (1999). FE Modelling of Mining-Induced Energy Release and Storage Rates. *J. South Afr. Inst. Mining Metall.* 99 (2), 103–110.

Napier, J. A. L. (1991). Energy Changes in a Rockmass Containing Multiple Discontinuities. *J. South Afr. Inst. Mining Metall.* 91 (5), 145–157.

Read, R. S. (2004). 20 Years of Excavation Response Studies at AECL's Underground Research Laboratory. *Int. J. Rock Mech. Mining Sci.* 41 (8), 1251–1275. doi:10.1016/j.ijrmms.2004.09.012

Revuzhenkor, A. F., and Klishin, S. V. (2009). Energy Flux Lines in a Deformable Rock Mass with Elliptical Openings. *J. Min Sci.* 45 (3), 201–206. doi:10.1007/s10913-009-0026-5

Salamon, M. D. G. (1984). Energy Considerations in Rock Mechanics: Fundamental Results. *J. South Afr. Inst. Mining Metall.* 84 (8), 233–246. doi:10.1016/0022-3115(84)90073-4

Salamon, M. D. G. (1983). *Rockburst hazard and the Fight for its Alleviation in South African Gold Mines, Proc. Rockbursts Prediction and Control*. London: IMM, 11–36.

Singh, S. P. (1988). Burst Energy Release Index. *Rock Mech. Rock Engng.* 21 (2), 149–155. doi:10.1007/bf01043119

Solecki, R., and Conant, R. J. (2003). *Advanced Mechanics of Materials*. London: Oxford University Press.

Su, G., Jiang, J., Feng, X., Jiang, Q., Chen, Z., and Mo, J. (2018). Influence of Loading Rate on Strainburst: an Experimental Study. *Bull. Eng. Geol. Environ.* 78 (5), 3559–3573. doi:10.1007/s10064-018-1351-1

Su, G., Zhai, S., Jiang, J., Zhang, G., and Yan, L. (2017). Influence of Radial Stress Gradient on Strainbursts: an Experimental Study. *Rock Mech. Rock Eng.* 50 (10), 2659–2676. doi:10.1007/s00603-017-1266-3

Toksöz, M. N., and Kehrer, H. H. (1972). Tectonic Strain Release by Underground Nuclear Explosions and its Effect on Seismic Discrimination. *Geophys. J. Int.* 31 (1-3), 141–161. doi:10.1111/j.1365-246X.1972.tb02364.x

Walsh, J. B. (1977). Energy Changes Due to Mining. *Int. J. Rock Mech. Mining Sci. Geomechanics Abstr.* 14 (1), 25–33. doi:10.1016/0148-9062(77)90559-9

Wang, J.-A., and Park, H. D. (2001). Comprehensive Prediction of Rockburst Based on Analysis of Strain Energy in Rocks. *Tunnelling Underground Space Technology.* 16 (1), 49–57. doi:10.1016/S0886-7798(01)00030-X

Wawersik, W. R., and Fairhurst, C. (1970). A Study of Brittle Rock Fracture in Laboratory Compression Experiments. *Int. J. Rock Mech. Mining Sci. Geomechanics Abstr.* 7 (5), 561–575. doi:10.1016/0148-9062(70)90007-0

Xie, H. P., Ju, Y., and Li, L. Y. (2005). Criteria for Strength and Structural Failure of Rocks Based on Energy Dissipation and Energy Release Principles. *Chin. J. Rock Mech. Eng.* 24 (17), 3003–3010. doi:10.1007/s11769-005-0030-x

Yang, J. H., Jiang, Q. H., Zhang, Q. B., and Zhao, J. (2018). Dynamic Stress Adjustment and Rock Damage During Blasting Excavation in a Deep-Buried Circular Tunnel. *Tunnelling Underground Space Technology.* 71, 591–604. doi:10.1016/j.tust.2017.10.010

Yang, J., Lu, W., Jiang, Q., Yao, C., Jiang, S., and Tian, L. (2016). A Study on the Vibration Frequency of Blasting Excavation in Highly Stressed Rock Masses. *Rock Mech. Rock Eng.* 49 (7), 2825–2843. doi:10.1007/s00603-016-0964-6

Zhang, C. S., Chen, X. R., Hou, J., and Chu, W. J. (2010). Study of Mechanical Behavior of Deep-Buried Marble at JinPing II Hydropower Station. *Chin. J. Rock Mech. Eng.* 29 (10), 1999–2009.

Zhu, W. C., Wei, J., Zhao, J., and Niu, L. L. (2014). 2D Numerical Simulation on Excavation Damaged Zone Induced by Dynamic Stress Redistribution. *Tunnelling Underground Space Technology.* 43, 315–326. doi:10.1016/j.tust.2014.05.023

Conflict of Interest: Author ZL is employed by China Gezhouba Group Explosive Co. Ltd.

The remaining authors declare that the research was conducted in the absence of any commercial or financial relationships that could be construed as a potential conflict of interest.